*Korean J. Chem. Eng.*, 39(4), 986-996 (2022)
DOI: 10.1007/s11814-021-0997-8

pISSN: 0256-1115
eISSN: 1975-7220

# Modification of hollow BiOCl/$TiO_2$ nanotubes with phosphoric acid to enhance their photocatalytic performance

**Guozhe Sui*,**,†, Yulin Zhang*, Jinlong Li*,**,†, Yan Zhuang*, Dongxuan Guo*,**, Ze Luo*, Rongping Xu*, Shuang Liang*, Hong Yao*, and Chao Wang***

*College of Chemistry and Chemical Engineering, Qiqihar University, Qiqihar 161006, P. R. China
**Heilongjiang Provincial Key Laboratory of Catalytic Synthesis for Fine Chemicals, Qiqihar University, Qiqihar 161006, P. R. China
(*Received 25 August 2021 • Revised 21 October 2021 • Accepted 27 October 2021*)

**Abstract**−Organic pollutants in dyed wastewater are hazardous to human health and the environment. The photocatalytic degradation of pollutants is considered a green treatment with significant social and environmental benefits. In this study, hollow BiOCl/$TiO_2$ nanotubes with open pores at both ends, prepared by hydrothermal synthesis, were modified using phosphoric acid to promote photoelectron transfer. The hollow nanotubes offer an increased number of electroactive sites, which enhances the photoelectric transfer efficiency and reduces the electron-hole recombination rate. The modification by $H_3PO_4$ significantly optimized the photocatalytic activity of the nanotubes. The results show that the $H_3PO_4$ modified hollow BiOCl/$TiO_2$ (molar ratio of BiOCl to $TiO_2$ is 0.8) nanotubes exhibited the most efficient photocatalytic performance toward rhodamine B (RhB) with a photodegradation efficiency of up to 98.8% under visible-light illumination. These nanotubes have broad application prospects for the effective removal of organic pollutants from wastewater and can potentially inform future research on photocatalysts.

Keywords: Hollow BiOCl/$TiO_2$ Nanotubes, Visible Light Illumination, Photocatalysis, Phosphoric Acid

## INTRODUCTION

The rapid development of science and industrial technology has led to an increase in the efficiency and productivity of modern industries and the happiness index of people [1-4]. At the same time, our environment has undergone significant changes. Serious water pollution has been caused by the discharge of persistent and toxic dyes, including anthraquinone, indigoide, triphenylmethyl, xanthene, azo derivatives, and so on. Such wastewater is characterized by strong color, high amounts of total dissolved solids (TDS), high chemical oxygen demand (COD), highly fluctuating pH, and low biodegradability, and has directly and indirectly threatened human health [5]. Therefore, it is particularly important to identify an effective remedy for water pollution. There are many technical methods for removing dye wastewater, as shown in Table 1, such as adsorption, membrane separation and filtration, ozonation, and activated sludge degradation [5,6]. However, photocatalytic technology, which involves a relatively advanced oxidation process (AOP), is a topic of intensive research in the field of environmental pollution treatment, especially the degradation of pollutants in water [7]. Bismuth oxychloride (BiOCl) with an optical indirect band gap of 3.46 eV is an attractive p-type semiconductor with stable physical and chemical properties, in which the Cl 3p and Bi 6p states occupy the highest occupied molecular orbital (HOMO) and the lowest unoccupied

**Table 1. Technical methods for removing dye wastewater [5]**

| Method | Advantages | Limitation |
|---|---|---|
| Adsorption | Simple operation, wide application | High cost, rapid saturation of adsorbents |
| Coagulation | High efficiency, simple operation | High production of sludge |
| Fenton process | High efficiency, inexpensive Fenton's reagent | Production of sludge, acidic condition |
| Photocatalysis | No sludge | Inefficient in high concentration, high energy consumption |
| Ozonation | Application for gaseous state, no change in volume | Short half-life, production of by-products |
| Membrane | Wide application, high-quality water | High production of sludge, high pressure, high cost |
| Biological process | Public treatment, cost benefit | Slow reaction, high cost for maintenance, low efficiency for complicated dyes |

†To whom correspondence should be addressed.
E-mail: gzhsui@qqhru.edu.cn, jinlong141@163.com

molecular orbital (LUMO), respectively. BiOCl has played a significant role in photocatalytic degradation and has attracted widespread attention owing to its open crystal structure and indirect optical transition performance [8-10].

To further improve the performance of BiOCl towards the photocatalytic degradation of pollutants in water, extensive research has been conducted on the preparation and morphology of the catalysts. $TiO_2$ is typically used in conjunction with BiOCl to develop composites with enhanced photocatalytic performance. Hu et al. synthesized a novel $TiO_2$ and BiOCl laminar composite material by the hydrolysis precipitation method, which exhibited significantly improved separation efficiency of charges and enhanced response to visible light [11]. Wang et al. synthesized a BiOCl and $TiO_2$ composite catalyst with a flower-like structure by a one-step alcohol heating method that exhibited high photocatalytic degradation efficiency toward tetracycline hydrochloride, ofloxacin, and their mixtures [12]. Because of their larger specific surface area, higher electron transfer efficiency, and stronger photocatalytic performance, BiOCl and $TiO_2$ composite catalysts with different structures and morphologies have been prepared and studied. Notable structures include rod-like, lamellar, spherical, and flower-like structures [13]. The hollow tubular structure of the $TiO_2$ semiconductor material was found to be superior to other morphologies. The electron flow rate and photocatalytic performance are superior if the two ends of the hollow tubular structure are open [14-16]. Tong et al. synthesized $TiO_2$ with different morphologies using different methods and found that the hollow tubular structure exhibited enhanced specific surface area and electron-hole separation rates compared to other morphologies [17]. Bao et al. constructed hollow nanotube composite materials from BiOCl and $TiO_2$ through electrospinning, solvothermal, and calcination processes, which showed improved photocatalytic degradation effects due to the high adsorption capacity and efficiency of separation of electron-hole pairs compared to other morphologies owing to its special tubular structure [18]. However, the photocatalytic performance of the composites based on BiOCl and $TiO_2$ needs further improvement.

In this study, hollow $TiO_2$ nanotubes with open pores at both ends loaded with inorganic BiOCl particles have been developed. The composite material made of BiOCl/$TiO_2$ has a special heterostructure and delivers excellent photocatalytic performance. The synthesized hollow BiOCl/$TiO_2$ nanotubes were modified using an inorganic acid, phosphoric acid, to further enhance the photocatalytic performance of the composite material. To investigate the photocatalytic performance of the obtained composite material, rhodamine B (RhB) was used as a model pollutant in aqueous solutions under visible-light irradiation. The roles of phosphoric acid modification and the structure of the hollow nanotubes with open pores at both ends in the improvement of the photocatalytic activity and stability were investigated. The findings demonstrate a viable strategy for fabricating functionalized and structured BiOCl/$TiO_2$ composite photocatalysts with improved performance.

## EXPERIMENTAL

### 1. Chemicals

All chemical reagents were purchased from Sigma Aldrich Co. and were of analytical grade and used as received without further purification. Tetrabutyl titanate ($C_{16}H_{36}O_4Ti$, TBT) was used as the Ti source for synthesizing the hollow $TiO_2$ nanotubes, and bismuth (III) nitrate pentahydrate ($Bi(NO_3)_3{\cdot}5H_2O$) and potassium chloride (KCl) were used as the Bi and Cl sources, respectively, for the BiOCl samples. Additional reagents used were absolute ethanol ($C_2H_5OH$), ethylene glycol ($(CH_2OH)_2$), sodium bicarbonate ($NaHCO_3$), p-benzoquinone (BQ), tert-butanol (TBA), sodium hydroxide (NaOH), hydrochloric acid (HCl), and phosphoric acid ($H_3PO_4$).

### 2. Preparation of Hollow $TiO_2$ Nanotubes

NaOH solution (20 mL, 10 mol·$L^{-1}$) and 10 mL TBT were mixed gradually and stirred continuously for approximately 30 min at a constant speed. The resulting solution was transferred to a Teflon-lined autoclave and maintained at 150 °C for 24 h. Then, the obtained sample was acidified with 10 mL of 0.1 mol·$L^{-1}$ HCl for 30 min. After acidification and centrifugation, the obtained products were washed to neutrality with deionized water. Finally, the hollow $TiO_2$ nanotubes were obtained after drying and calcinating at a high temperature of 550 °C for 2 h.

### 3. Preparation of Hollow BiOCl/$TiO_2$ Nanotubes

Hollow BiOCl/$TiO_2$ nanotubes were prepared via in situ hydrothermal synthesis. First, 0.24 g of $TiO_2$ hollow nanotubes was dispersed in 10 mL ethanol, followed by sonication for approximately 1 h to form solution A. $Bi(NO_3)_3{\cdot}5H_2O$ (0.15 g) was mixed in 10 mL of ethanol and stirred for approximately 30 min, and then 3 mL of 0.1 mol·$L^{-1}$ HCl and 0.1 g KCl were added to form solution B. Next, solution B was slowly added to solution A followed by stirring for approximately 30 min to obtain solution C (molar ratio: BiOCl/$TiO_2$=1). Solution C was transferred to an autoclave and placed in a drying oven at 180 °C for 5 h. After centrifugation and washing to neutrality, the obtained sample was dried at 60 °C overnight to obtain hollow BiOCl/$TiO_2$ nanotubes. Hollow BiOCl/$TiO_2$ nanotubes with different molar ratios were prepared by varying the quantities of $Bi(NO_3)_3{\cdot}5H_2O$ and KCl. The obtained samples were labeled as BT-$x$ ($x$=0.6, 0.8, 1.0).

### 4. Modification of Hollow BiOCl/$TiO_2$ Nanotubes by $H_3PO_4$

The hollow BiOCl/$TiO_2$ nanotubes were modified using $H_3PO_4$ via the immersion method. For this, 10 mL of 1.0 mol·$L^{-1}$ $H_3PO_4$ and 0.25 g of BT-$x$ were mixed and stirred for approximately 30 min. Finally, the obtained products were centrifuged, washed to neutrality, and dried at 60 °C overnight. The hollow BiOCl/$TiO_2$ nanotubes modified using $H_3PO_4$ were labeled as HP-1.0-BT-$x$ ($x$=0.6, 0.8, 1.0).

### 5. Characterization

A Bruker D8 (Germany) with Cu K$\alpha$ radiation at 40 kV and an emission current of 200 mA was used to perform X-ray diffraction (XRD) analysis to measure the composition and crystal phase structure of the catalyst sample at a scanning speed of 4°·$min^{-1}$. A Hitachi S-4300 cold field emission scanning electron microscope (Japan) was used to perform scanning electron microscopy (SEM) at a voltage of 20 kV and an accelerating voltage of 5 kV. Transmission electron microscopy (TEM) was performed using a Hitachi H-7650 system (Japan) with an accelerating voltage of 100 kV. Ultraviolet (UV) spectroscopy was performed using a TU-1901 UV-visible spectrometer (China) with a barium sulfate ($BaSO_4$) tablet as the reference sample substrate in the wavelength range of 200-

800 nm. The specific surface area, pore volume, and other parameters of the samples were determined using an $N_2$ adsorption-desorption apparatus Nova 2000e (America) over the relative pressure range of 0.05-0.35. X-ray photoelectron spectroscopy (XPS) analysis was performed using an Axis Ultra DLD (UK) with a photoelectron take-off angle of 45°, and a measured voltage of 14.0 kV was used to detect the element types and element valence states of the semiconductor catalyst samples. Fourier-transform infrared (FT-IR) spectra were measured using a Nexus 670 (America) instrument using the KBr pellet technique.

**6. Photocatalytic Activity of Catalysts**

To evaluate the photocatalytic activity of the synthesized composite catalysts, RhB in an aqueous liquid was used as the model pollutant under visible-light irradiation. A 500 W xenon lamp was used instead of a visible light source, and a cut-off filter (>420 nm) was used to restrict the wavelength to the visible region. The synthesized catalyst (50 mg) and 50 mL of RhB solution (5 $mg \cdot L^{-1}$) were added to the tube reactor. Prior to irradiation with visible light for each measurement, the reaction solution containing the photocatalyst and RhB was mixed for 30 min in the dark to achieve adsorption-desorption equilibrium of RhB on the test sample. Aliquots of the solution samples were withdrawn from the tube reactor at intervals of 10 min and centrifuged each time using a high-speed centrifuge rotor to remove the suspended photocatalysts. The absorbance of the filtrate, measured using UV-visible spectrophotometry at 552 nm, was used to calculate the photocatalytic degradation efficiency of the synthesized composite catalysts toward RhB. Mineralization of RhB was determined by calculating total organic carbon (TOC) content using a TOC analyzer (Japan). To investigate the mechanism of the photocatalytic reaction, the active species of the reaction were determined by adding 0.1 $mol \cdot L^{-1}$ $NaHCO_3$, 0.4 $mmol \cdot L^{-1}$ BQ, and 0.1 $mol \cdot L^{-1}$ TBA. Finally, the reusability of the hollow HP-1.0-BT-*x* nanotube composite catalyst was determined by the cyclic photocatalytic degradation of fresh RhB solutions after repeated centrifugation and washing with ethanol. Bi leaching test was conducted by measuring the Bi content in degraded RhB solution via atomic absorption spectroscopy ICE-3500 (America).

## RESULTS AND DISCUSSION

**1. Characterization Analysis**

The XRD analysis results of the hollow $TiO_2$ nanotubes, BiOCl nanoparticles, BT-*x* (*x*=0.6, 0.8, 1.0), and HP-1.0-BT-0.8 composite catalysts are shown in Fig. 1. Diffraction peaks corresponding to pure $TiO_2$ were observed at 25.28°, 38.02°, 48.04°, 54.12°, 62.64°, 69.59°, and 75.14° corresponding to the (101), (004), (200), (211), (204), (220), and (215) crystal planes, respectively, of the anatase phase (JCPDS no.21-1272) [19]. The characteristic peaks of pure BiOCl nanoparticles appeared at 12.00°, 24.10°, 25.90°, 32.50°, 33.50°, 40.90°, 46.70°, 49.70°, 54.10°, 55.10°, and 58.60° corresponding to the (001), (002), (101), (110), (102), (112), (200), (113), (211), (104), and (212) crystal planes, respectively (JCPDS no. 85-0861), which indicated that the pure BiOCl nanoparticles had a tetragonal crystal structure [20]. The characteristic diffraction peaks of pure $TiO_2$ and BiOCl can be clearly seen in the BT-*x* and HP-1.0-BT-0.8 composite catalysts, which are different from those of pure $TiO_2$ and BiOCl. The strengthening of the diffraction peaks of the BT-x (*x*=0.6, 0.8, 1.0) composite catalysts at 32.5° and 33.5° was attributed to a negative effect on the migration distance of the photo-induced carriers. It was demonstrated that a heterogeneous structure was formed in BT-*x*. The intensity of some diffraction peaks of the HP-1.0-BT-0.8 composite catalyst is significantly weakened, which may be due to the introduction of phosphate ions, which reduces the strength of the peaks corresponding to the (001), (101), (110), and (102) crystal planes [21]. Under the action of the electrostatic force field, the photogenerated electrons and holes of the composite catalyst are effectively separated and transferred, and the migration distance of the photo-induced carriers is enhanced to a certain extent.

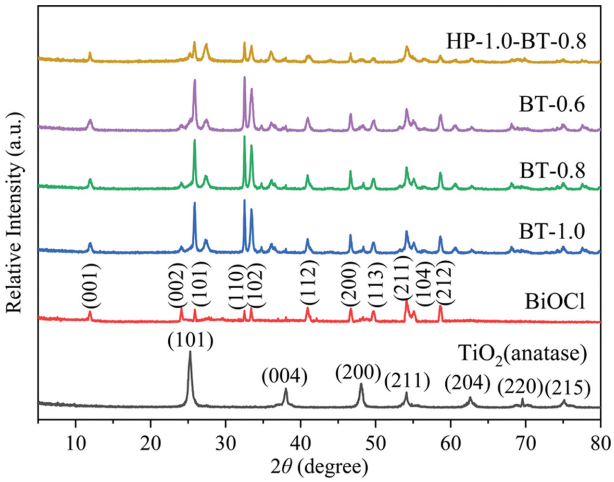


**Fig. 1. XRD spectra of pure hollow $TiO_2$ nanotube, BiOCl nanoparticle, BT-*x* (*x*=0.6, 0.8, 1.0) and HP-1.0-BT-0.8 composites.**

SEM and elemental analysis were performed to determine the morphology of the photocatalysts, and the results are shown in Fig. 2. It can be seen from Fig. 2(a) that a pure $TiO_2$ sample has a curved tubular shape with a length of approximately 100-200 nm. According to Fig. 2(b), the BiOCl nanoparticles measured approximately 20 nm, and exhibited slight agglomeration. Fig. 2(c) illustrates the SEM image of the HP-1.0-BT-0.8 composite material, and it is clear that the BiOCl nanoparticles adhered preferentially to the $TiO_2$ nanotubes. The adhesion of BiOCl nanoparticles is conducive to the formation of a stable heterojunction surface, which can produce a superior plasmon resonance effect. As shown in Fig. 2(e)-(i), elemental Ti, O, Bi, Cl, and P were sparsely and evenly distributed on the surface of HP-1.0-BT-0.8, which is consistent with the outline of the SEM image of HP-1.0-BT-0.8, as shown in Fig. 2(d).

TEM and high resolution (HR) TEM analyses were performed to demonstrate the presence of hollow nanotubes that were open at both ends in the HP-1.0-BT-0.8 composite catalyst, and the results are shown in Fig. 3. It can be clearly seen from Fig. 3(a) that the synthesized $TiO_2$ has a hollow tubular structure open at both ends. The tubular structure with a length of approximately 100-200 nm is relatively concentrated, consistent with the SEM results. As shown in Fig. 3(b), the average diameter of the BiOCl particles was approxi-

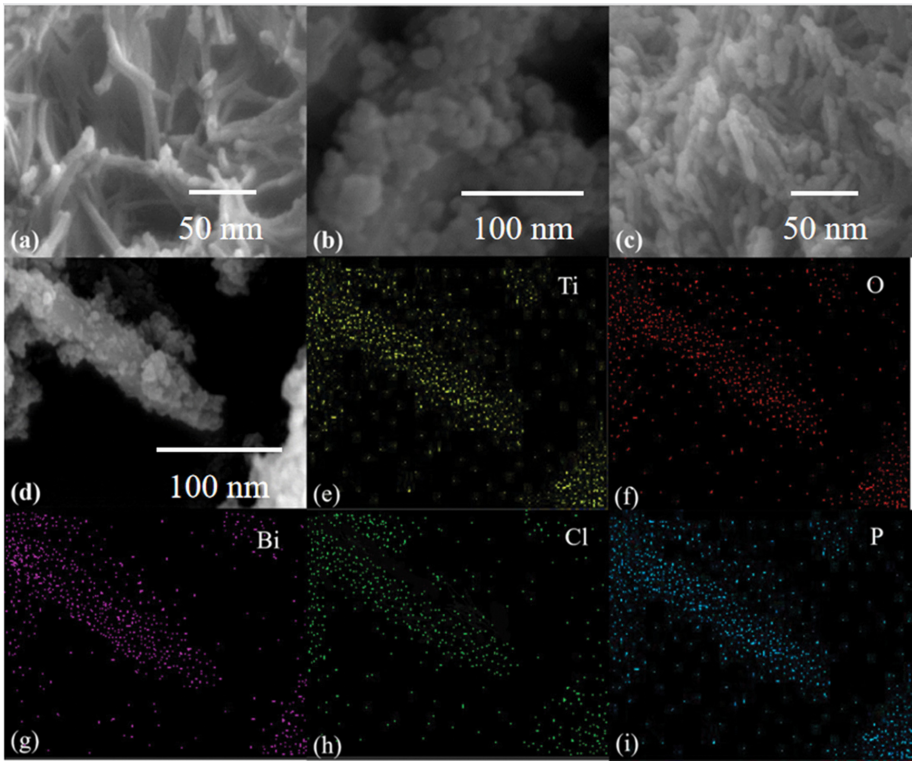


**Fig. 2. SEM images of (a) hollow $TiO_2$ nanotube, (b) BiOCl nanoparticles, (c) HP-1.0-BT-0.8 composite catalyst, SEM image of (d) HP-1.0-BT-0.8 composite catalyst, and element mapping of (e) Ti, (f) O, (g) Bi, (h) Cl and (i) P for HP-1.0-BT-0.8 composite catalyst.**

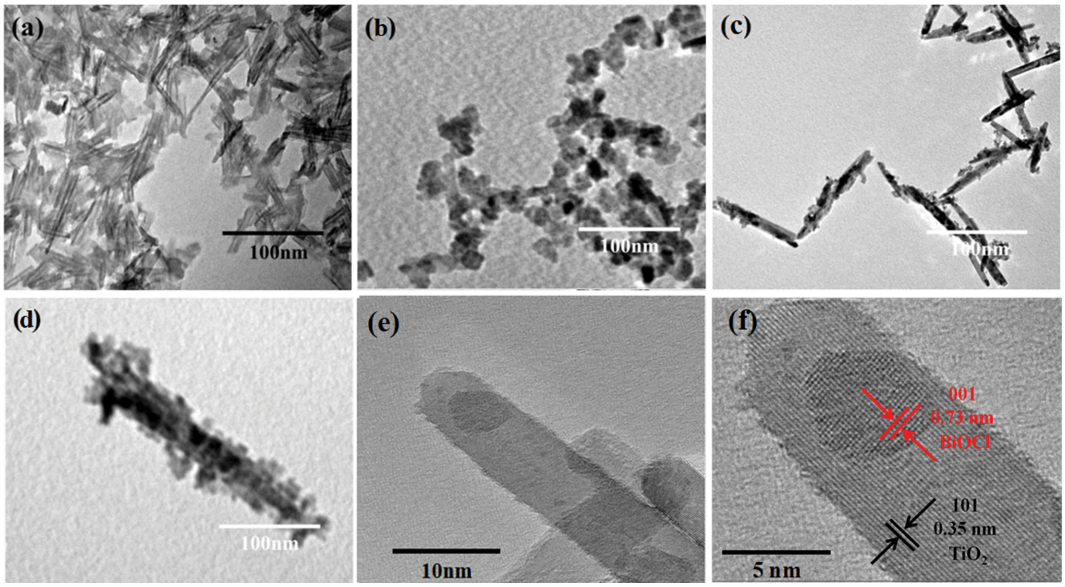


**Fig. 3. TEM images of (a) hollow $TiO_2$ nanotube, (b) BiOCl nanoparticles, (c) and (d) HP-1.0-BT-0.8, and HRTEM images of HP-1.0-BT-0.8 composite catalyst.**

mately 20 nm; however, particle aggregation was observed. These BiOCl nanoparticles formed composites with the hollow $TiO_2$ nanotubes. As can be seen from Fig. 3(c) and (d), the BiOCl nanoparticles were uniformly dispersed on the surface of the hollow $TiO_2$ nanotubes, indicating that the BiOCl nanoparticles and hollow $TiO_2$ nanotubes were successfully composited to form a heterostructure.

HRTEM micrographs of the HP-1.0-BT-0.8 composite catalyst are shown in Fig. 3(e) and (f). It can be seen that the planar lattice spacing of BiOCl is 0.73 nm, which corresponds to the (001) crystal plane [22]. The distance corresponding to the (101) crystal plane of anatase $TiO_2$ was 0.35 nm [23]. These results correspond with the conclusions obtained from XRD analysis. It was demonstrated

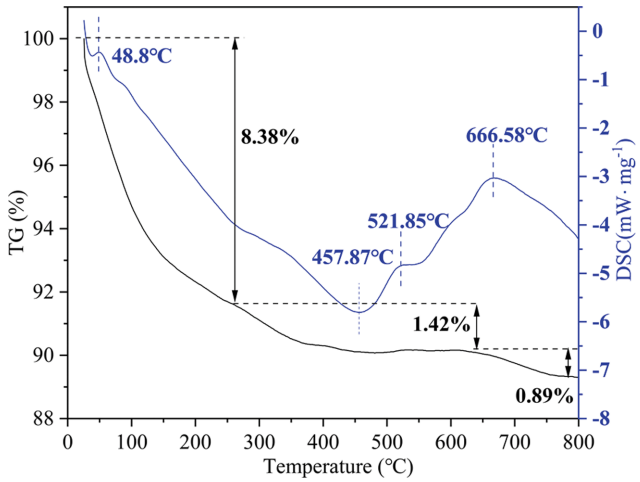


**Fig. 4. TG-DSC curve chart of HP-1.0-BT-0.8 composite catalyst.**

that BiOCl and $TiO_2$ successfully formed a heterojunction catalyst with hollow nanotubes open at both ends.

Fig. 4 shows the TG-differential scanning calorimetry (DSC) curve of the HP-1.0-BT-0.8 composite catalyst. Clearly, there are three weight loss regions in the TG curve in the range of 0-800 °C. The first weight loss of 8.38% occurred between 20 and 260 °C, mainly due to the dehydration of adsorbed water from the HP-1.0-BT-0.8 composite catalyst via continuous heating [24]; the second weight loss of 1.42% occurred between 260 and 500 °C, corresponding to the endothermic peak at 521.85 °C and the exothermic peak at 457.87 °C, mainly due to the loss of structural water and the decomposition of $H_3PO_4$ in the HP-1.0-BT-0.8 composite [25]; the third weight loss of 0.89% occurred between 640 and 800 °C, corresponding to the endothermic peak at 666.58 °C, mainly due to the transformation of the crystal type caused by high-temperature changes in the HP-1.0-BT-0.8 composite [26]. The total weight loss during the entire sintering process was 10.69%, which was less than the theoretical weight loss. This is mainly due to the relatively stable structure and performance of the HP-1.0-BT-0.8 composite catalyst.

Fig. 5 shows the $N_2$ adsorption isotherms and pore size distribution curves of the hollow $TiO_2$ nanotubes, BiOCl nanoparticles, BT-*x* (*x*=0.6, 0.8, 1.0), and HP-1.0-BT-0.8 composites. The prepared samples exhibited Type IV isotherm curves with H1-type hysteresis loops, as shown in Fig. 5(a). The HP-1.0-BT-0.8 composite catalyst had a mesoporous structure, and its pore size was distributed in the range of 5-12 nm (Fig. 5(b)). Table 2 shows the specific surface area (SBET), pore diameter (BJH), and pore volume of each catalyst. According to these data, the pure hollow $TiO_2$ nanotubes have the largest specific surface area (approximately 133.72 $m^2 \cdot g^{-1}$).

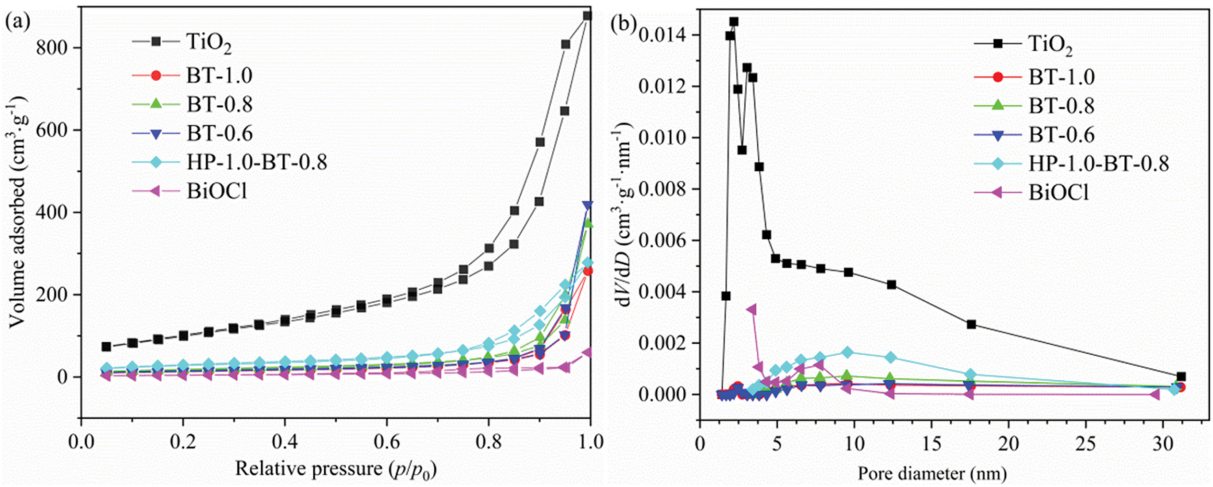


**Fig. 5. (a) $N_2$ adsorption-desorption isotherms and (b) corresponding pore size distribution map of hollow $TiO_2$ nanotube, BiOCl nanoparticles, BT-*x* (*x*=0.6, 0.8, 1.0) and HP-1.0-BT-0.8 composites.**

**Table 2. The specific surface area, pore size, pore volume size and band gap of hollow $TiO_2$ nanotube, BiOCl nanoparticles, BT-*x* (*x*=0.6, 0.8, 1.0) and HP-1.0-BT-0.8 composites**

| Samples | Specific surface area ($m^2 \cdot g^{-1}$) | Pore volume ($cm^3 \cdot g^{-1}$) | Average pore size (nm) | Band gap $E_g$ (eV) |
|---|---|---|---|---|
| $TiO_2$ | 133.72 | 1.27 | 5.88 | 3.41 |
| BiOCl | 24.54 | 0.04 | 3.18 | 3.32 |
| BT-0.6 | 47.54 | 0.25 | 10.95 | 2.78 |
| BT-0.8 | 62.82 | 0.31 | 9.84 | 2.56 |
| BT-1.0 | 47.68 | 0.26 | 10.73 | 2.95 |
| HP-1.0-BT-0.8 | 92.51 | 0.34 | 7.39 | 2.46 |

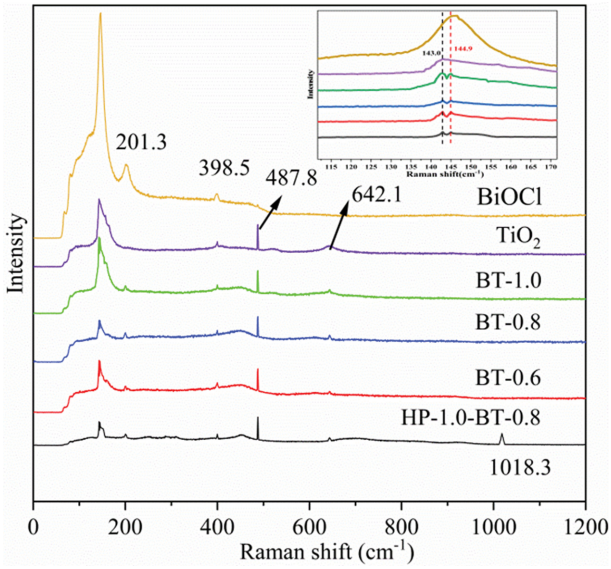


**Fig. 6. Raman spectra of hollow $TiO_2$ nanotube, BiOCl nanoparticles, BT-*x* (*x*=0.6, 0.8, 1.0) and HP-1.0-BT-0.8 composites.**

This may be due to the special structure of the hollow $TiO_2$ nanotubes, which is consistent with the TEM results [27,28]. The specific surface area of the HP-1.0-BT-0.8 composite catalyst was larger, which provided more active sites for the photocatalytic reaction.

Fig. 6 shows the Raman spectra of the hollow $TiO_2$ nanotubes, BiOCl nanoparticles, BT-*x* (*x*=0.6, 0.8, 1.0), and HP-1.0-BT-0.8 composites. Characteristic peaks of anatase $TiO_2$ were observed at 143, 398.5, 487.8, and 642.1 $cm^{-1}$ in the Raman spectrum of the hollow $TiO_2$ nanotubes, which is consistent with the conclusions from XRD analysis [29]. Characteristic peaks at 144.9, 201.3, and 398.5 $cm^{-1}$ appear in BiOCl [30]. These characteristic peaks appear in the synthesized BT-*x* (*x*=0.6, 0.8, 1.0) and HP-1.0-BT-0.8 composite catalysts. The magnified image in the upper right corner of the figure shows the presence of two peaks at 143 and 144.9 $cm^{-1}$, which proves the formation of a heterojunction structure. The peak at 143 $cm^{-1}$ corresponding to $H_3PO_4$ gradually became weaker, which may be due to the defects induced in the crystal lattice [31]. Compared with the hollow $TiO_2$ nanotubes, the peak at 642.1 $cm^{-1}$ of HP-1.0-BT-0.8 exhibited a certain red shift. As the wavelength increased, the frequency decreased, leading to weakening of the vibration [32]. In addition, a new peak appeared at 1,018.3 $cm^{-1}$ in the HP-1.0-BT-0.8 composite catalyst, which was due to the introduction of phosphate ($PO_4^{3-}$) [33].

XPS was performed to determine the elemental composition and electronic structure of the HP-1.0-BT-0.8 composite catalyst. The results are shown in Fig. 7. The spectrum (Fig. 7(a)) clearly shows that the HP-1.0-BT-0.8 composite catalyst comprises five elements: Bi, O, Cl, Ti, and P. In the energy spectrum of Bi (Fig. 7(b)), two signal peaks are located at 159.18 and 164.46 eV, corresponding to the two split orbitals of Bi $4f_{7/2}$ and Bi $4f_{5/2}$, respectively [34]. The difference between the $Bi^{3+}$ peaks is approximately 5.3 eV, which is characteristic of the mixed BiOCl sample [35]. In Fig. 7(c), two signal peaks are observed at 197.8 and 199.39 eV, corresponding to the two split orbitals of Cl $2p_{3/2}$ and Cl $2p_{1/2}$ [36]. In Fig. 7(d), one major O 1s peak is observed at 531.55 eV corresponding to the Ti-O-Ti and Bi-O bonds [37], while the other peak at 532.44 eV may be closely related to the O-H bonds in water adsorbed on the surface [38]. Fig. 7(e) shows the peaks of Ti 2p at 459.97 and 466.17 eV corresponding to Ti $2p_{3/2}$ and Ti $2p_{1/2}$, respectively [39]. The difference between the two signal peaks is approximately 6.2 eV, indicating that Ti exists as $Ti^{4+}$ [40]. The peak at 531.55 eV corresponds to Ti-O bonds, which is consistent with the results shown in Fig. 7(d) [41]. As can be seen in Fig. 7(f), the strong peak at 133.31 eV, corresponding to the P-O bond, indicates that P exists in the form of $PO_4^{3-}$ [42].

Fig. 8(a) shows the UV-vis diffuse reflectance spectra of the hollow $TiO_2$ nanotubes, BiOCl nanoparticles, BT-*x* (*x*=0.6, 0.8, 1.0), and HP-1.0-BT-0.8 composites. The absorption-edge wavelength of the pure hollow $TiO_2$ nanotube catalyst sample with open holes at both ends is approximately 385-390 nm, which leads to a wider response wavelength range compared with pure $TiO_2$, mainly because hollow nanotubes with open pores can enhance the transport efficiency of photoelectrons. The special structure of the hollow tube leads to accelerated photoelectron movement and improved response to light-irradiation [43]. Compared with the hollow $TiO_2$ nanotubes and BiOCl nanoparticles, the light absorption wavelengths of the BT-*x* (*x*=0.6, 0.8, 1) and HP-1.0-BT-0.8 composites show a significant change, which indicates that the open-pored hollow $TiO_2$ nanotubes and BiOCl nanoparticles formed a heterogeneous structure. In particular, the absorption of HP-1.0-BT-0.8 shifted to the visible range. This is mainly due to the synergistic effect of the heterostructure between the hollow nanotubes with open pores and the large number of active sites provided by $H_3PO_4$ [44]. As shown in Fig. 8(b), compared with the band gaps of hollow $TiO_2$ nanotubes (3.41 eV) and BiOCl nanoparticles (3.32 eV), the band gaps of the BT-0.6, BT-0.8, and BT-1 composite catalysts reduced to 2.78, 2.56, and 2.95 eV, respectively. The band gap of the HP-1.0-BT-0.8 catalyst is 2.46 eV, which is the narrowest. This is mainly because the introduction of phosphate increases the number of active sites, improves the photoelectron transfer efficiency, and inhibits the recombination of electron-hole pairs between the catalysts [45].

To study the migration, transfer, and recombination of photogenerated electron-hole pairs in the composite catalyst, a photoluminescence test was performed on the catalyst, and the results are shown in Fig. 9. The highest absorption peaks of pure hollow $TiO_2$ nanotubes appeared at 452 and 470 nm in the photoluminescence spectrum [46]. The peak intensity of BT-0.8 was slightly reduced after BiOCl was compounded with the $TiO_2$ nanotubes. In addition, the peak intensity of HP1.0-BT-0.8 significantly reduced due to the introduction of $H_3PO_4$, which accelerated the migration of photogenerated electron-hole pairs. The decrease in the photoluminescence intensity indicates a decrease in the recombination rate of electron-hole pairs. The stronger the photogenerated electron capture ability, the higher the photogenerated carrier separation efficiency [47]. This is beneficial for improving the photocatalytic activity of the composite catalyst, which is consistent with the photocatalytic activity results.

**2. Photocatalytic Performance**

In this experiment, RhB was used as the model pollutant to

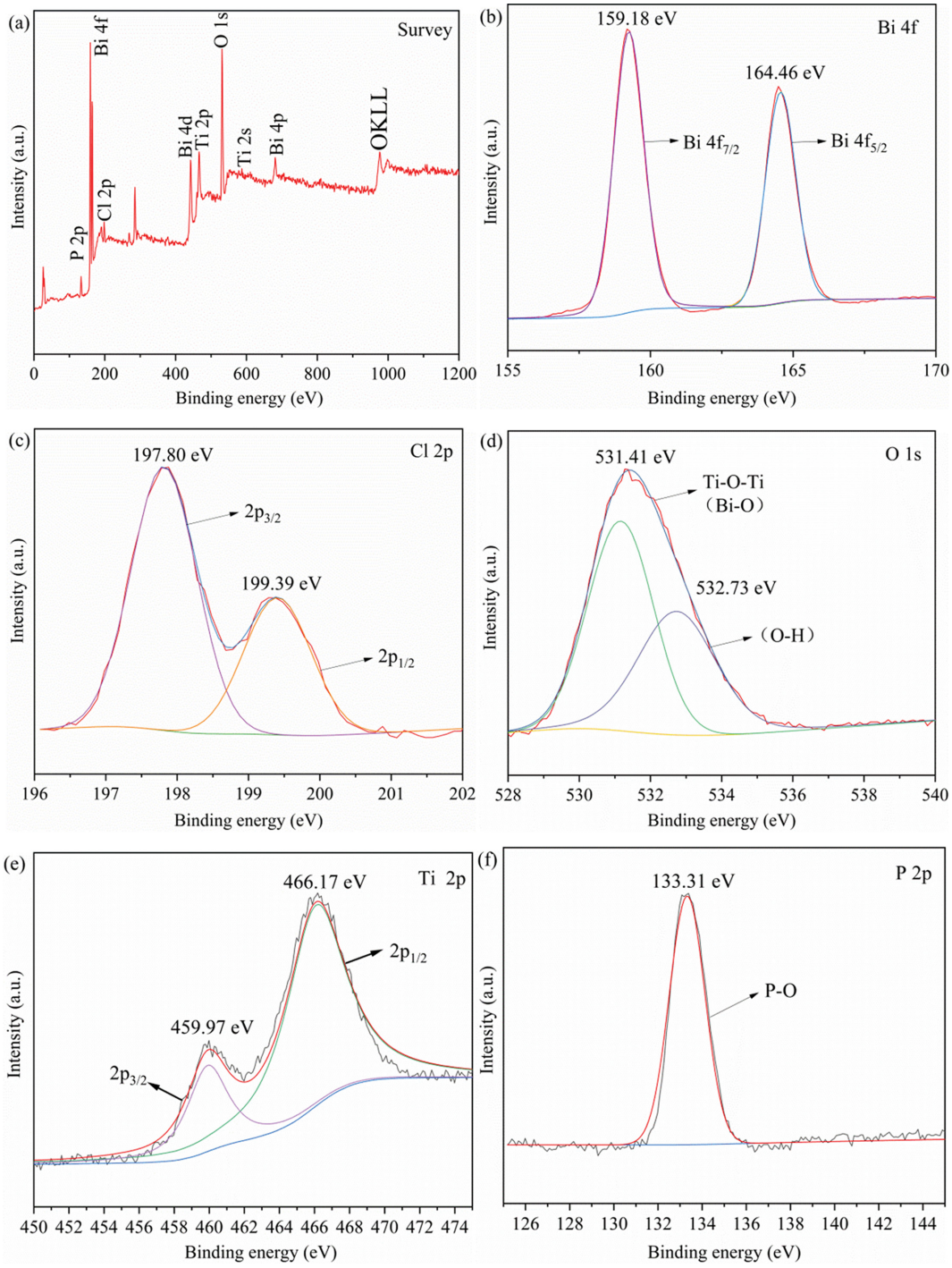


**Fig. 7. XPS spectra of (a) full spectrum, (b) Bi 4f, (c) Cl 2p, (d) O 1s, (e) Ti 2p, and (f) P 2p for HP-1.0-BT-0.8 composite catalyst.**

degrade the photocatalytic activity of the hollow $TiO_2$ nanotubes, BiOCl nanoparticles, BT-$x$ ($x$=0.6, 0.8, 1.0), and HP-1.0-BT-0.8 composites, and the results are shown in Fig. 10. Fig. 10(a) shows the degradation rate curve of each photocatalyst. As shown, almost no concentration change of RhB was observed without any photocatalysts, while RhB was degraded gradually with the presence of photocatalysts. The degradation efficiency of the hollow $TiO_2$ nanotubes and BiOCl nanoparticles toward RhB was 78.5% and 83.3%, respectively, within 110 min under visible-light illumination. The degradation efficiency of the BT composite catalysts was significantly improved; notably, the degradation efficiency of the HP1.0-BT-0.8 composite catalyst reached 98.8%, which was 1.3 and 1.2 times that of the hollow $TiO_2$ nanotubes and BiOCl nanoparticles, respectively. Photocatalytic mineralization degrees of RhB by different catalysts after 110 min visible light illumination were investigated by TOC analysis as shown in Table 3. The HP1.0-BT-0.8 composite catalyst exhibited the highest mineralization degree (76.3%), which was higher than that of the hollow $TiO_2$ nanotubes (58.4%)

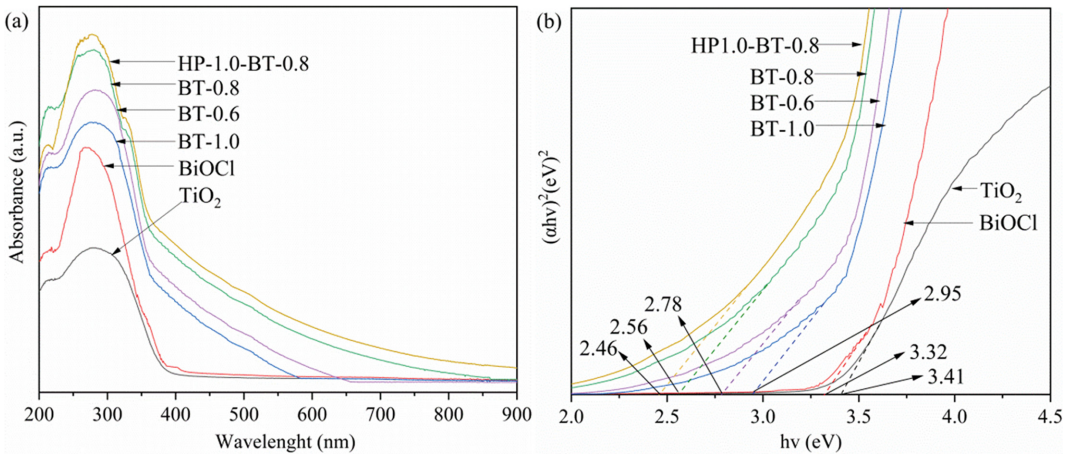


**Fig. 8. (a) UV-vis diffuse reflectance spectra and (b) $(\alpha hv)^2$ and energy hv relationship diagram of hollow $TiO_2$ nanotube, BiOCl nanoparticles, BT-*x* (*x*=0.6, 0.8, 1.0) and HP-1.0-BT-0.8 composites.**

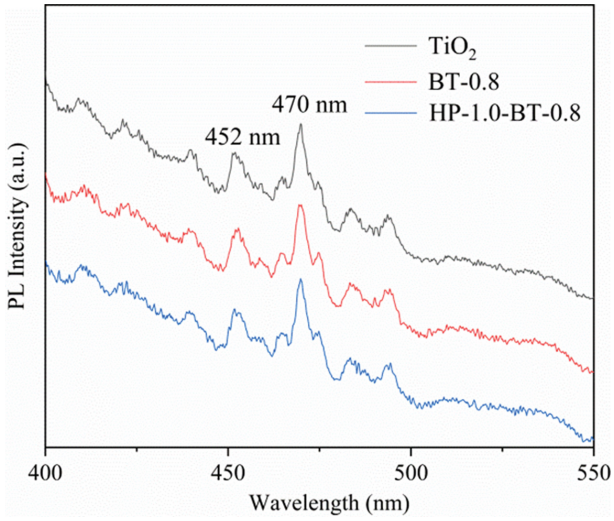


**Fig. 9. PL spectra of hollow $TiO_2$ nanotube, BT-0.8, and HP-1.0-BT-0.8 composite catalyst.**

and BiOCl nanoparticles (62.3%), indicating that the HP1.0-BT-0.8 composite catalyst had better mineralization. This is mainly because modification using phosphoric acid and the hollow nanotube structures supplied with open pores provided more active sites due to the interface effect, which accelerated the transportation of electrons between the catalysts [48].

In addition, the photocatalytic degradation process conformed to the pseudo-first-order kinetic model, as shown in Fig. 10(b). The rate constants for RhB degradation by the different catalysts were calculated using the equation shown in Fig. 10(c). The rate constant k of the photodegradation reaction in presence of the HP-1.0-BT-0.8 composite catalyst is $4.063\times10^{-2}$ $min^{-1}$, which is 2.9 and 2.5 times higher than that in presence of the hollow $TiO_2$ nanotubes ($1.396\times10^{-2}$ $min^{-1}$) and BiOCl nanoparticles ($1.625\times10^{-2}$ $min^{-1}$), respectively. This is because the synergistic effect in the HP-1.0-BT-0.8 composite catalyst effectively improved the photoelectron transfer efficiency and inhibited rapid electron-hole recombination [49]. The influence of the initial solution pH on the photocatalytic performance of HP-1.0-BT-0.8 was investigated to determine the acidity difference of different systems. It can be deduced from Fig. 10(d) that the photocatalytic degradation efficiency of RhB increased by HP-1.0-BT-0.8 with a decrease in initial solution pH. This is because RhB readily ionizes in acidic solution for weakly alkaline dye and then interacts with acidified HP-1.0-BT-0.8 photocatalyst. To explore its stability and recyclability, seven repeated cycles of the HP1.0-BT-0.8 catalyst washing with an ethanol solution were performed, as shown in Fig. 10(e). The degradation efficiency of HP-1.0-BT-0.8 toward RhB decreased from 98.8% to 89.4% under visible light illumination for 110 min after seven cycles, indicating that HP-1.0-BT-0.8 exhibited better stability. To investigate the stability of HP-1.0-BT-0.8 further, the Bi leaching test was conducted after a 110-min visible light illumination. The amount of Bi leached into the solution was measured by atomic absorption spectroscopy (0.05814 $mg\cdot g^{-1}$), which was 0.201% compared with the amounts of Bi in HP-1.0-BT-0.8, indicating that HP-1.0-BT-0.8 has good stability. The HP-1.0-BT-0.8 catalyst can thus be used for the degradation of organics in wastewater.

To determine the contribution of holes ($h^+$), hydroxyl free radicals (•OH), and superoxide radicals ($\bullet O^{2-}$) species in RhB degradation, $NaHCO_3$, BQ, and TBA were selected as radical scavengers [50]. TBA can react rapidly with •OH ($k=(3.8-7.6)\times10^8$ $M^{-1}\cdot s^{-1}$ and BQ quench $\bullet O^{2-}$ ($k=9.6\times10^8$ $M^{-1}\cdot s^{-1}$); in contrast, $NaHCO_3$ can act as a scavenger of $h^+$ and •OH ($k=8.5\times10^6$ $M^{-1}\cdot s^{-1}$) [51]. As depicted in Fig. 10(f), the degradation efficiency of the HP-1.0-BT-0.8 composite catalyst toward RhB under visible irradiation was reduced from 98.8% to 94.1%, 44.4%, and 35.3% in the pres-

**Table 3. Mineralization degrees of RhB by different catalysts after 110 min visible light illumination**

| Samples | $TiO_2$ | BiOCl | BT-0.6 | BT-0.8 | BT-1.0 | HP-1.0-BT-0.8 |
|---|---|---|---|---|---|---|
| Mineralization degree | 58.4% | 62.3% | 66.5% | 73.6% | 70.2% | 76.3% |

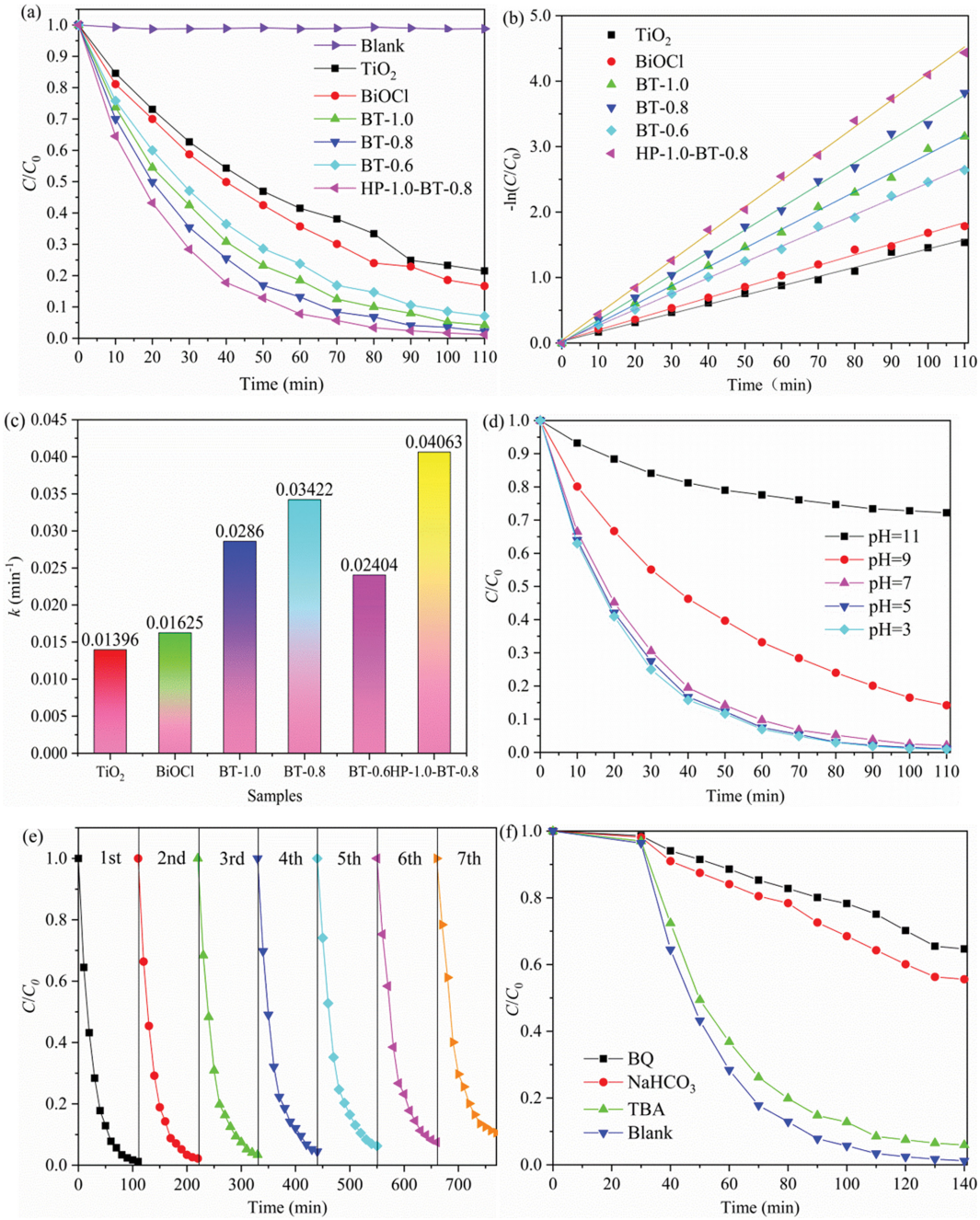


**Fig. 10. (a) Photocatalytic degradation of RhB under visible light irradiation, (b) kinetic curves of RhB degradation, (c) pseudo-first-order rate constant k of each catalyst, (d) influence of initial solution pH on the photocatalytic performance of HP-1.0-BT-0.8, (e) recycling of HP-1.0-BT-0.8 in the removal of RhB, and (f) scavenger test results obtained using HP-1.0-BT-0.8.**

ence of TBA, $NaHCO_3$, and BQ, respectively, indicating that $\bullet O^{2-}$ and $h^+$ are the principal active species in the photocatalytic degradation of RhB.

## 3. Proposed Mechanism of Photocatalytic Degradation

A mechanism underlying the photocatalytic degradation of RhB by HP-1.0-BT-0.8 was proposed, as illustrated in Fig. 11. The energies of the valence band (VB) and conduction band (CB) were calculated as follows [52]:

$$E_{VB}=X-E_e+0.5E_g \quad (1)$$

$$E_{CB}=E_{VB}-E_g \quad (2)$$

where $E_g$ is the band gap energy of the catalyst [eV], X is the absolute electronegativity of the semiconductor [eV], and $E_e$ is the free electron energy based on hydrogen (4.5 eV).

The VB and CB edge potentials of $TiO_2$ are calculated from Eqs. (1) and (2) as 3.02 eV and −0.4 eV, respectively. The VB and CB edge potentials of BiOCl are 3.52 eV and 0.2 eV, respectively.

Under visible light irradiation, RhB absorbed on the surface of BiOCl acts as a photosensitizer, which can be directly excited. The

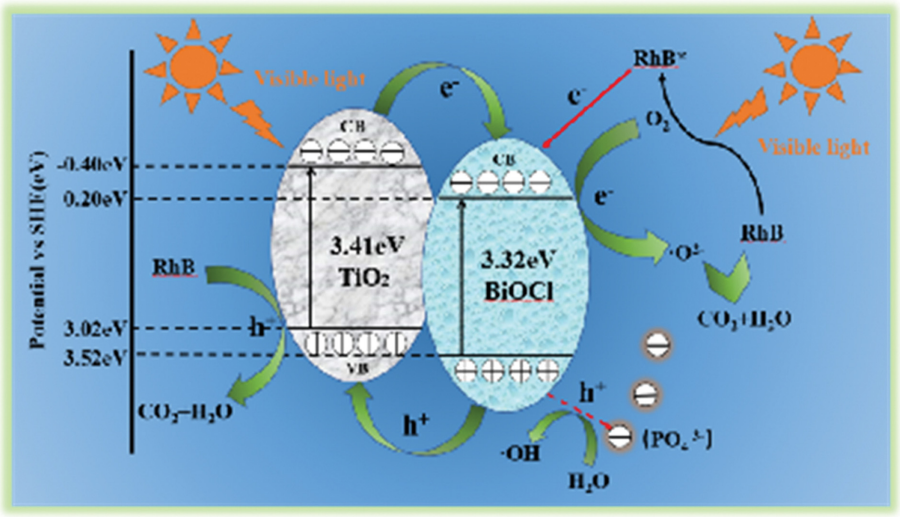


**Fig. 11. Photocatalytic degradation mechanism of HP-1.0-BT-0.8 composite catalyst.**

VB electrons excited to the CB (marked as RhB*) absorbed the dissolved oxygen ($O_2$) in the solution, followed by complete reaction with oxygen to form superoxide radicals, $\bullet O^{2-}$, which continue to react with RhB to form carbon dioxide, water, and other substances [53]. The $h^+$ generated upon excitation of the $TiO_2$ semiconductor are oxidized by RhB, which gets degraded and finally converted to carbon dioxide, water, and other substances. In addition, $PO_4^{3-}$ reacts with the holes $h^+$ to produce •OH and water. The holes $h^+$ react with water to produce •OH. The production of •OH generates a synergistic effect that promotes degradation [54]. The heterogeneous interface between BiOCl and $TiO_2$ is equivalent to that of the newly formed electron transfer channel. The CB electrons of $TiO_2$ are transferred to the CB of BiOCl, and the VB electrons of BiOCl are transferred to the VB of $TiO_2$. Transfer to the VB of $TiO_2$ accelerates the electron-transfer between BiOCl and $TiO_2$, and effectively inhibits the recombination and combination of photogenerated electron-hole pairs. The introduction of phosphate also plays a role in optimization.

## CONCLUSION

BiOCl/$TiO_2$ heterojunction composite catalysts modified by phosphoric acid (HP-1.0-BT-*x*), comprising hollow nanotubes with open pores at both ends, were successfully prepared by the solvothermal and *in situ* hydrothermal techniques. The hollow $TiO_2$ nanotube structure with openings at both ends increased the specific surface area of the catalyst and enhanced its photocatalytic activity. In addition, BiOCl with the (001) crystal plane provided more oxygen vacancies, which is highly useful for photocatalytic degradation. Owing to the formation of a heterogeneous interface between the BiOCl and $TiO_2$ materials, more heterogeneous active sites were exposed, and the transfer of interface electrons was promoted, which effectively inhibited the rapid recombination of electrons and holes between BiOCl and $TiO_2$. Upon modification using $H_3PO_4$, the photocatalytic performance of the composite catalyst was further optimized, and the photocatalytic degradation efficiency of the HP-1.0-BT-0.8 composite catalyst, which had the most effective composite ratio, toward RhB reached 98.8% under visible light illumination for 110 min, which was 2.9 times and 2.5 times that of pure hollow $TiO_2$ nanotubes and BiOCl nanoparticles, respectively. Therefore, this study not only provides an improved design principle for photocatalysts but also an efficient tool for the photocatalytic degradation of organics in wastewater.

## ACKNOWLEDGEMENTS

This work was supported by the Research Project of Education Ministry of Heilongjiang Province of China (135409401, 135409101).

## CONFLICT OF INTEREST

There is no conflict of interest.

## REFERENCES

1. H. Wang, X. T. Hu, Y. J. Ma, D. J. Zhu, T. Li and J. Y. Wang, *Chin. J. Catal.*, **41**, 95 (2020).
2. C. Wang, G. Z. Sui, D. X. Guo, J. L. Li, L. Zhang, S. B. Li, J. J. Xin, D. F. Chai and W. X. Guo, *J. Colloid Interf. Sci.*, **599**, 577 (2021).
3. U. Farooq, M. Sajid, A. Shan, X. H. Wang and S. G. Lyu, *Chem. Eng. J.*, **423**, 130221 (2021).
4. J. L. Li, S. Q. Jia, G. Z. Sui and L. J. Du, *Chem. Pap.*, **72**, 369 (2018).
5. F. Ghanbari and M. Moradi, Boca Raton: CRC Press (2016).
6. M. S. Ur Rehman, I. Kim, N. Rashid, M. A. Umer, M. Sajid and J. I. Han, *Clean-Soil Air Water*, **44**, 55 (2016).
7. G. Luna-Sanguino, A. Tolosana-Moranchel, J. Carbajo, L. Pascual, A. Rey, M. Faraldos and A. Bahamonde, *Mol. Catal.*, **493**, 111059 (2020).
8. H. H. Liu, J. Huang, J. F. Chen, J. B. Zhong, J. Z. Li and D. M. Ma, *Chem. Phys. Lett.*, **748**, 137401 (2020).
9. L. Q. Ye, X. L. Jin, Y. M. Leng, Y. R. Su, H. Q. Xie and C. Liu, *J. Power Sources*, **293**, 409 (2015).

10. H. B. Yu, D. Ge, Y. P. Liu, Y. Lu, X. H. Wang, M. X. Huo and W. C. Qin, *Sep. Purif. Technol.*, **251**, 117414 (2020).
11. X. L. Hu, C. Q. Li, J. Y. Song, S. L. Zheng and Z. M. Sun, *J. Colloid Interf. Sci.*, **574**, 61 (2020).
12. Q. Wang, P. J. Li, Z. Zhang, C. Y. Jiang, K. C. Zuojiao, J. X. Liu and Y. P. Wang, *J. Photoch. Photobiol. A*, **378**, 114 (2019).
13. L. Li, M. Y. Zhang, Y. Liu and X. T. Zhang, *J. Colloid Interf. Sci.*, **435**, 26 (2014).
14. X. F. Qu, Y. D. Yi, F. Y. Qiao, M. H. Liu, X. R. Wang, H. H. Meng, L. Shi and F. L. Du, *Ceram. Int.*, **44**, 1348 (2018).
15. H. Y. Li, J. F. Liu, J. J. Qian, Q. Y. Li and J. J. Yang, *Chin. J. Catal.*, **35**, 1578 (2014).
16. J. L. Li, D. S. Zhen, G. Z. Sui, C. M. Zhang, Q. G. Deng and L. H. Jia, *J. Nanosci. Nanotech.*, **12**, 6265 (2012).
17. X. Tong, W. H. Shen, X. Q. Chen and J. P. Corriou, *Ceram. Int.*, **43**, 14200 (2017).
18. S. R. Q. Q. G. Bao, H. O. Liang, C. P. Li and J. Bai, *J. Photoch. Photobiol. A*, **397**, 112590 (2020).
19. G. Z. Sui, J. L. Li, T. Liu, T. T. Zhao, Z. L. Hao, D. S. Zhen, J. Lv, L. H. Jia and T. Jing, *Mater. Express*, **6**, 1 (2016).
20. Z. Li, B. J. Ma, X. F. Zhang, Y. H. Sang and H. Liu, *Environ. Res.*, **182**, 109077 (2019).
21. H. H. Liu, C. Yang, J. Huang, J. F. Chen, J. B. Zhong and J. Z. Li, *Inorg. Chem. Commun.*, **113**, 107806 (2020).
22. J. Zhang, K. Zhu, Y. K. Zhu, C. C. Qin, L. Y. Liu, Y. J. Wang, W. Gan, X. C. Fu and H. Q. Hao, *Chem. Phys. Lett.*, **750**, 137483 (2020).
23. J. Tian, Z. Y. Chen, J. P. Jing, C. Feng, M. M. Sun and W. B. Li, *Mater. Lett.*, **272**, 127860 (2020).
24. G. X. Zhang, Z. M. Sun, X. L. Hu, A. K. Song and S. L. Zheng, *J. Taiwan Inst. Chem. E.*, **81**, 435 (2017).
25. U. Alam, M. Fleisch, I. Kretschmer, D. Bahnemann and M. Muneer, *Appl. Catal. B-Environ.*, **218**, 758 (2017).
26. Z. Q. Cheng, S. Z. Zhao, L. J. Kang, M. T. Li and Z. L. Gao, *Mater. Lett.*, **214**, 80 (2017).
27. S. J. Yao, J. Wang, X. X. Zhou, S. S. Zhou and X. P. Pu, *Adv. Powder Technol.*, **31**, 1924 (2020).
28. Z. Wang, A. Mahmood, X. F. Xie, X. Wang, H. X. Qiu and J. Sun, *Chem. Engin. J.*, **393**, 124723 (2020).
29. J. L. Li, T. Liu, G. Z. Sui and D. S. Zhen, *J. Nanosci. Nanotech.*, **15**, 1408 (2015).
30. Q. Liu, J. F. Ma, K. Wang, T. Feng, M. G. Peng, Z. S. Yao, C. H. Fan and S. Komarneni, *Ceram. Int.*, **43**, 5751 (2017).
31. Y. H. Shen, X. Yu, W. T. Lin, Y. Zhu and Y. M. Zhang, *Appl. Surf. Sci.*, **399**, 67 (2017).
32. W. M. Zhou, J. Wang, X. G. Wang, J. F. Li, Y. Li and C. W. Wang, *Opt. Mater.*, **99**, 109567 (2020).
33. Y. Tian, C. F. Guo, Y. J. Guo, Q. Wang and Q. Liu, *Appl. Surf. Sci.*, **258**, 1949 (2012).
34. Q. Jiang, W. L. Xie, S. Y. Han, Y. F. Wang and Y. Zhang, *Colloid Surf. A*, **583**, 123962 (2019).
35. D. W. Li, Y. Wang, J. J. Zhou, J. C. Wang, X. Y. Liu, Y. Y. Tian, Z. B. Zhang, Y. Y. Qiao, L. Wei, J. H. Li and L. Wen, *Mater. Lett.*, **230**, 61 (2018).
36. Z. B. Zhang, X. Y. Liu, D. W. Li, T. T. Gao, Y. Q. Lei, B. G. Wu, J. W. Zhao, Y. K. Wang and L. Wei, *Carbon*, **144**, 841 (2019).
37. R. R. Fu, X. Q. Zeng, L. Ma, S. M. Gao, Q. Y. Wang, Z. Y. Wang, B. B. Huang, Y. Dai and J. Lu, *J. Power Sources*, **312**, 12 (2016).
38. K. X. Wang, C. L. Shao, X. H. Li, X. Zhang, N. Lu, F. J. Miao and Y. C. Liu, *Catal. Commun.*, **67**, 6 (2015).
39. S. Q. Jia, J. L. Li, G. Z. Sui, L. J. Du, Y. L. Zhang, Y. Zhuang and B. X. Li, *RSC Adv.*, **9**, 31177 (2019).
40. J. L. Li, L. J. Du, S. Q. Jia, G. Z. Sui, Y. L. Zhang, Y. Zhuang, B. X. Li and Z. Y. Xing, *RSC Adv.*, **8**, 29654 (2018).
41. M. D. Sikora, A. V. Rosario, E. C. Pereira and C. O. Paiva-Santos, *Electrochim. Acta*, **56**, 3122 (2011).
42. L. L. Zhang, J. H. Zhang, W. G. Zhang, J. Q. Liu, H. Zhong and Y. J. Zhao, *Mater. Res. Bull.*, **66**, 109 (2015).
43. J. L. Li, Y. Zhuang, G. Z. Sui, D. X. Guo, Y. L. Zhang, Z. Luo, R. P. Xu, S. Liang and H. Yao, *Ionics*, **27**, 3185 (2021).
44. X. Liu, C. Q. He, X. J. Yu, Y. T. Bai, L. Ye, B. S. Wang and L. F. Zhang, *Powder Technol.*, **326**, 181 (2018).
45. Z. H. Jia, T. Li, Z. F. Zheng, J. D. Zhang, J. X. Liu, Y. W. Wang, X. C. Zhang, Y. F. Wang and C. M. Fan, *Chem. Eng. J.*, **380**, 122422 (2020).
46. J. L. Li, B. X. Li, G. Z. Sui, L. J. Du, Y. Zhuang, Y. L. Zhang and Y. F. Zou, *J. Mol. Struct.*, **1231**, 130023 (2021).
47. C. Wang, G. Z. Sui, D. X. Guo, J. L. Li, L. Zhang, S. B. Li, J. J. Xin, D. F. Chai and Y. Huang, *Ionics*, **27**, 1723 (2021).
48. B. C. Cao, P. Y. Dong, S. Cao and Y. H. Wang, *J. Am. Ceram. Soc.*, **44**, 544 (2013).
49. F. Dong, T. Xiong, S. Yan, H. Q. Wang, Y. J. Sun, Y. X. Zhang, H. W. Huang and Z. B. Wu, *J. Catal.*, **344**, 401 (2016).
50. X. D. Tang, C. S. Ma, N. Liu, C. L. Liu and S. L. Liu, *Chem. Phys. Lett.*, **709**, 82 (2018).
51. S. Giannakis, K. Y. A. Lin and F. Ghanbari, *Chem. Eng. J.*, **406**, 127083 (2021).
52. J. L. Li, S. Q. Jia, G. Z. Sui, L. J. Du and B. X. Li, *RSC Adv.*, **7**, 34857 (2017).
53. A. Mohseni-Bandpei, S. M. Ghasemi, A. Eslami, M. Rafiee, M. Sadani and F. Ghanbari, *J. Photoch. Photobio. A*, **418**, 113425 (2021).
54. G. Z. Sui, J. L. Li, L. J. Du, Y. Zhuang, Y. L. Zhang, Y. F. Zou and B. X. Li, *J. Alloys Compd.*, **283**, 153851 (2020).